Available online at www.sciencedirect.com
ScienceDirect
International Journal of Heat and Mass Transfer 51 (2008) 1810–1817
International Journal of HEAT and MASS TRANSFER
www.elsevier.com/locate/ijhmt

Effect of pool rotation on flow pattern transition of silicon melt thermocapillary flow in a slowly rotating shallow annular pool

You-Rong Li [a,*], Lan Xiao [a], Shuang-Ying Wu [a], Nobuyuki Imaishi [b]

[a] College of Power Engineering, Chongqing University, Chongqing 400044, China
[b] Institute for Materials Chemistry and Engineering, Kyushu University, Fukuoka, Japan

Received 10 October 2006; received in revised form 28 June 2007
Available online 20 August 2007

Abstract

In order to understand the mechanism of the flow pattern transitions on silicon melt in Czochralski furnaces, we conducted a series of unsteady three-dimensional numerical simulations of silicon melt flow in a slowly rotating shallow annular pool in the counter-clockwise direction. The pool was heated from the outer cylinder and cooled at the inner cylinder. The temperature differences between the vertical outer and inner cylinders ranged from 5 K to 28 K and annular pool rotation rate from 0 and 2 rpm. Bottom and top surfaces of the melt pool were adiabatic. The simulation results indicate that two flow transitions occur when increasing the radial temperature difference along the free surface. At first, the steady two-dimensional flow becomes the first hydrothermal wave and then the second hydrothermal wave with less wave number. The critical conditions for the onset of the instability and the transition zone between the first and the second hydrothermal wave are determined at various rotation rates. Characteristics of the steady and the three-dimensional flows are discussed.

Keywords: Computer simulation; Thermocapillary flow; Hydrothermal wave; Rotation; Silicon melt

1. Introduction

It is well known that understanding transition to oscillatory thermocapillary flows is important to material processing. In the past few decades, there have been a large number of linear stability analyses, experimental and numerical studies of surface tension driven convection in open rectangular and annular pools. Smith and Davis [1] performed a linear stability analysis of a thin and infinitely extended fluid layer with a free upper surface subjected to a horizontal temperature gradient. They found two types of three-dimensional (3D) instabilities, i.e. stationary longitudinal rolls and oblique hydrothermal waves (HW) depending on the Prandtl number (Pr) and the basic flow pattern, and determined the critical Marangoni number. Garnier and Normand [2] carried out a linear stability analysis of radial thermocapillary flow in an extended cylindrical geometry for liquids with $Pr = 10$ and predicted that the instability appears first near the inner cylinder. Subsequently, Zebib [3] showed the influence of rotation on thermocapillary instabilities by a linear stability analysis of a parallel flow model and found that the Coriolis force must be included in thermocapillary simulations. Le Cunff and Zebib [4] confirmed the significance of the Coriolis effects on thermocapillary instabilities in a liquid bridge of infinite length.

On the other hand, numerous experiments of thermocapillary flows in open cavities and annular pools are available. Kamotani et al. [5–7] conducted many microgravity experiments on the oscillatory thermocapillary flow of silicone oil in open cylindrical containers with cylindrical diameters of 12, 20, and 30 mm, in which the liquid was heated either by a hot solid cylinder located at the pool axis or by a laser beam. They observed two or three lobed surface temperature patterns. Mukolobwiez et al. [8] observed HWs traveling in the azimuthal direction in a shallow

* Corresponding author. Tel.: +86 23 6511 2284; fax: +86 23 6510 2473.
E-mail address: liyourong@cqu.edu.cn (Y.-R. Li).

0017-9310/$ - see front matter © 2007 Elsevier Ltd. All rights reserved.
doi:10.1016/j.ijheatmasstransfer.2007.06.029

Nomenclature

d	depth, m
$\boldsymbol{e}_z$	z-directional unit vector
f	frequency, Hz
g	gravitational acceleration, $g = 9.806\ \mathrm{m\ s^{-2}}$
m	azimuthal wave number
Ma	Marangoni number
n	rotation rate, rpm
p	pressure, Pa
Pr	Prandtl number
r	radius, m
t	time, s
T	temperature, K
v	velocity, $\mathrm{m\ s^{-1}}$
$\boldsymbol{v}$	velocity vector
z	axial coordinate, m

Greek symbols

α	thermal diffusivity, $\mathrm{m^2\ s^{-1}}$
β	growth rate constant
γ_T	temperature coefficient of surface tension, $\mathrm{N\ m^{-1}\ K^{-1}}$
θ	azimuthal coordinate, rad
μ	dynamic viscosity, $\mathrm{kg\ m^{-1}\ s^{-1}}$
ν	kinematic viscosity, $\mathrm{m^2\ s^{-1}}$
ρ	density, $\mathrm{kg\ m^{-3}}$
ρ_T	thermal expansion coefficient, $\mathrm{K^{-1}}$
ψ	stream function, $\mathrm{m^3/s}$

Subscripts

c	cold
cri	critical
h	hotter
i	inner
m	melting point
o	outer
r	radial
z	axial
θ	azimuthal

annular channel of silicone oil ($Pr = 10$) (depth of 1.7 mm, width of 10 mm, and mean radius of 80 mm) heated from the inner wall. To determine the influence of the depth on the wavelength of HWs, Schwabe et al. [9] conducted experiments on the thermocapillary flow in annular liquid pools of ethanol ($Pr = 17$) with a thickness of 0.6–3.6 mm (inner radius of 20 mm and outer radius of 77 mm), heated at the inner rod. They observed short-wavelength temperature patterns with curved arms (part of spirals) in shallow liquid pools ($d < 1.4$ mm) and long-wavelength temperature patterns in deeper pools ($d > 1.4$ mm). Garnier et al. [10] observed HWs with spiral-like arms in an annular container of silicone oil with the inner heated cylinder of radius $r_i = 4$ mm, the outer cooled container of radius $r_o = 67.5$ mm and the depth $d = 1.2$ mm or 1.9 mm. They also observed pulsating, target-like wave patterns (i.e., concentric circles traveling radially outward) dominant only near the cold inner wall and curved arms of HWs dominant in the entire area of the liquid pool. Subsequently, Schwabe et al. [11,12] studied experimentally thermocapillary flows of silicone oil in a Czochralski (Cz) model system and annular pool under normal gravity and micro-gravity. They observed hydrothermal waves traveling on the free surface for thin annular gaps, and found that the number of waves increases as the Marangoni (Ma) number increases. They also determined the critical conditions for the incipience of oscillations under various conditions, and recognized that gravity increased the critical Ma number. Fein and Pfeffer [13] investigated baroclinic waves in a rotating annulus experiment using a low-Prandtl number fluid (mercury $Pr = 0.0246$). They found that in mercury baroclinic waves have a drift direction counter to the annulus rotation in the low-rotation regime and a co-rotation in the high-rotation regime. Standing waves were also observed. Seidl et al. [14] presented the observations of azimuthal m-folded ($m = 2, 3, 4, \ldots$) wave patterns, both by experiments and numerical investigations. The experiments were performed in a silicon melt without a crystal. They found that the m-folded waves propagate in a direction opposite to the crucible at higher crucible rotation rates. The higher the crucible rotation rate, the faster the phase velocity of the wave. Nakamura [15] showed the thermal waves due to a nonaxisymmetric flow at a Czochralski-type silicon-melt surface with a carbon-dummy crystal. They found the thermal wave number increased as the crucible rotation rate increased and the rotation rate of the thermal wave was lower than the crucible rotation rate. Recently, Azami et al. [16] observed spoke patterns on the surface of a shallow, the Cz configuration pool of high-temperature silicon melt (3 mm and 8 mm in depth) and reported that thermocapillary flow may play an important role in the incipience of the 3D convection and the number of spokes.

Numerical simulations have carried out to understand the characteristics of thermocapillary convections. Sim and Zebib [17] reported 3D simulations of thermocapillary convection in an open cylindrical annulus. Four kinds of surface temperature patterns were observed with increasing Ma, i.e., two types of rotating patterns with two or three lobes, and two types of pulsating patterns with two or three lobes. Sim et al. [18] and Li et al. [19] conducted numerical simulations of thermocapillary flow in an annular pool of silicone oil for the same geometry as that of experiments of Schwabe et al. [11,12] on FOTON-12, and compared their results with the FOTON-12 microgravity experiments. Shi and Imaishi [20] reported the two-dimensional

(2D) and 3D numerical simulations of thermocapillary flow, as well as buoyant thermocapillary flow, in the same pool of silicone oil with the depth of 1.0 mm. With this small depth, they believed that the thermocapillary force was dominant and the buoyant force could be negligible. In our previous papers [21–23], unsteady 3D numerical simulations of thermocapillary and thermocapillary-buoyancy flow in annular pool of silicon melt ($Pr = 0.011$) and in shallow molten silicon pool with the Cz configuration were performed, respectively. In the present study, we report our results for effect of pool rotation on the flow pattern transition of thermocapillary flow in a rotating annular pool of silicon melt.

2. Model formulation

2.1. Basic assumptions and governing equations

We analyze the 3D flow of silicon melt in a shallow annular layer of depth d, inner radius r_i and outer radius r_o, with a free upper surface and solid bottom, as shown schematically in Fig. 1. The system rotates in the counter-clockwise direction at a constant rate n (rpm) about a vertical axis. The inner and outer cylinders are maintained at constant temperatures T_c and T_h, ($T_h > T_c$), respectively. The horizontal temperature gradient varies in the radial direction. Melt convection is generated by the surface tension gradient on the free surface and rotation of annular pool. The following assumptions are introduced in our model: (1) Silicon melt is an incompressible Newtonian fluid and a constant property assumption is applicable except for the surface tension and the density in the additional buoyancy term in the radial direction. (2) The velocity is small and the flow is laminar. (3) The upper surface is flat and nondeformable. (4) At the top free surface, the thermocapillary force is taken into account. At other solid–liquid boundaries, the no-slip condition is applied.

With the above assumptions, the flow and heat transfer equations in a fixed frame are expressed as follows:

$$\nabla \cdot \boldsymbol{v} = 0, \tag{1}$$

$$\frac{\partial \boldsymbol{v}}{\partial t} + \boldsymbol{v} \cdot \nabla \boldsymbol{v} = -\frac{1}{\rho}\nabla p + \nu \nabla^2 \boldsymbol{v} - \rho_T (T - T_m)\frac{v_\theta^2}{r}\boldsymbol{e}_r, \tag{2}$$

$$\frac{\partial T}{\partial t} + \boldsymbol{v} \cdot \nabla T = \alpha \nabla^2 T. \tag{3}$$

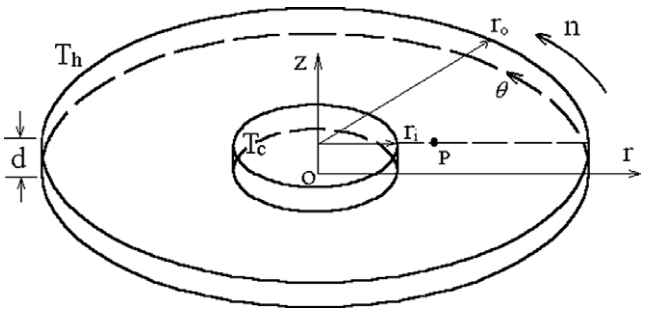

Fig. 1. Configuration of the system.

The boundary conditions at the free surface ($z = d$, $r_i < r < r_o$, $0 \leqslant \theta < 2\pi$),

$$\mu \frac{\partial v_r}{\partial z} = -\gamma_T \frac{\partial T}{\partial r}, \tag{4a}$$

$$\mu \frac{\partial v_\theta}{\partial z} = -\gamma_T \frac{\partial T}{r\partial \theta}, \tag{4b}$$

$$v_z = 0, \tag{4c}$$

$$\frac{\partial T}{\partial z} = 0. \tag{4d}$$

At the bottom ($z = 0$, $r_i < r < r_o$, $0 \leqslant \theta < 2\pi$),

$$v_r = 0, \tag{5a}$$

$$v_\theta = 2\pi n r/60, \tag{5b}$$

$$v_z = 0, \tag{5c}$$

$$\frac{\partial T}{\partial z} = 0. \tag{5d}$$

At the inner cylinder ($r = r_i$, $0 \leqslant z \leqslant d$, $0 \leqslant \theta < 2\pi$),

$$v_r = 0, \tag{6a}$$

$$v_\theta = 2\pi n r_i/60, \tag{6b}$$

$$v_z = 0, \tag{6c}$$

$$T = T_c = T_m. \tag{6d}$$

At the outer cylinder ($r = r_o$, $0 \leqslant z \leqslant d$, $0 \leqslant \theta < 2\pi$),

$$v_r = 0, \tag{7a}$$

$$v_\theta = 2\pi n r_o/60, \tag{7b}$$

$$v_z = 0, \tag{7c}$$

$$T = T_h. \tag{7d}$$

The initial conditions are expressed as follows (at $t = 0$):

$$v_r = 0, \tag{8a}$$

$$v_\theta = 0, \tag{8b}$$

$$v_z = 0, \tag{8c}$$

$$T = T_m + (T_h - T_m)\frac{\ln(r/r_i)}{\ln(r_o/r_i)}. \tag{8d}$$

2.2. Calculation conditions and numerical method

The geometric parameters for the simulation are $r_i = 15$ mm, $r_o = 50$ mm, $d = 3$ mm. The thermophysical properties of silicon melt used in this work are identical to those in Ref. [21]. The temperature differences ΔT between the vertical inner and outer cylinders ranged from 5 K to 28 K and annular pool rotation rate n from 0 and 2 rpm.

The fundamental equations are discretized by the control volume method with the modified central difference approximation in the diffusion terms, the QUICK scheme in the convective terms and an implicit method in time. The SIMPLER algorithm is used to handle the pressure–velocity coupling. The other descriptions of the mathematical model and numerical procedure can be found in Ref.

[21]. The validity of the code for the thermocapillary flow simulation has been well confirmed in Refs. [19–23].

3. Results and discussion

3.1. Basic flow

In the present configuration, the basic thermocapillary flow of silicon melt in the shallow annular layer appears as an axisymmetric steady radial flow with a single convection roll cell when $\Delta T \leqslant 1$ K at a low fixed rotation rate. The surface fluid flows from the hot outer cylinder to the cold inner cylinder. A return flow is present near the bottom. When ΔT is increased, a second co-rotating roll cell appears in melt layers, as shown in Fig. 2. The strength of the second co-rotating cell increases as ΔT increases. The annular pool rotation suppresses the basic flow. Compared Fig. 2a and b, it is found that the maximum stream function $\psi(+)$ decreases from 0.2 cm^3/s to 0.196 cm^3/s when rotation rate increases to 0.5 rpm. The stream function ψ is defined as

$$v_r = \frac{1}{r}\frac{\partial \psi}{\partial z}, \quad v_z = -\frac{1}{r}\frac{\partial \psi}{\partial r}.$$

At $n = 2$ rpm and $\Delta T = 12$ K, the third co-rotating cell is generated and a small counter-rotating cell appears near the bottom and inner cylinder of the pool, as shown in Fig. 2d. It is also found that the temperature distribution in the radial direction is almost independent of the presence of the annular pool rotation, since the thermal conductivity of the silicon melt is large.

When the annular pool rotates, the additional buoyancy in the radial direction is created by the non-uniform temperature distribution in the radial direction. We check the effect of this buoyancy term on the basic flow. Simulations with and without the additional buoyancy are performed for $n = 2$ rpm and $\Delta T = 12$ K. They produced almost same flow patterns and the error of the maximum stream functions is less than 1%. Therefore, the additional buoyancy term is uninfluenced on the basic flow.

3.2. Critical temperature differences ΔT_{cri}

If the annular pool is stationary ($n = 0$), any radial temperature difference ($\Delta T > 0$) produces a surface tension gradient on the free surface of the melt and the Marangoni effect induces flow in the melt layer. If ΔT exceeds a threshold value, the hydrothermal wave is formed in the melt layer, as discussed in Ref. [21]. When the annular pool rotates, present numerical simulations show that during the initial growth process the intensity of any disturbance (δX) can also be expressed by Eq. (9),

$$\delta X(r, \theta, z, t) = \delta X_0(r, \theta, z) \exp[(\beta + i\beta_I)t], \tag{9}$$

where β is the growth rate constant of the disturbance and β_I represents the time dependent oscillatory characteristics of the disturbance. The β value can be determined from the slope of the semi-logarithmic plot of $\delta v_{\theta,\max}$ vs. Δt. By plotting β vs ΔT, we can determine the critical temperature difference ΔT_{cri} and wave number m at various rotation rates, as shown in Table 1. Rotating solid walls exert a shear

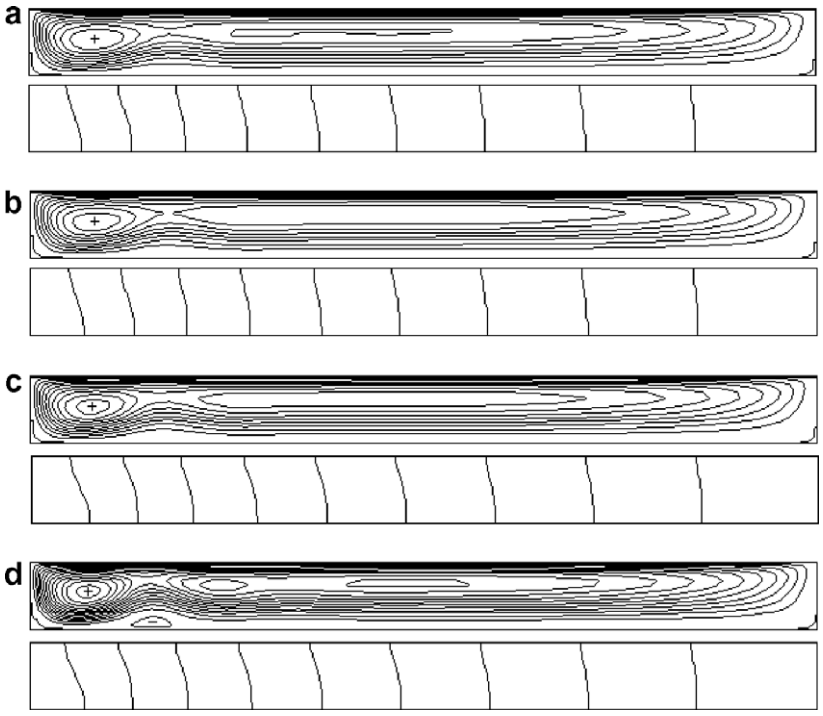

Fig. 2. Streamlines and isotherms in the melt below the critical temperature difference. $\delta\psi = 0.02$ cm^3/s. (a) $n = 0$ rpm, $\Delta T = 7$ K, $\psi(+) = 0.200$ cm^3/s, $\delta T = 0.7$ K. (b) $n = 0.5$ rpm, $\Delta T = 7$ K, $\psi(+) = 0.196$ cm^3/s, $\delta T = 0.7$ K. (c) $n = 1.0$ rpm, $\Delta T = 8$ K, $\psi(+) = 0.210$ cm^3/s, $\delta T = 0.8$ K. (d) $n = 2.0$ rpm, $\Delta T = 12$ K, $\psi(+) = 0.268$ cm^3/s, $\psi(-) = -0.002$ cm^3/s, $\delta T = 1.2$ K.

Table 1
The critical ΔT_{cri} and m

n (rpm)	ΔT_{cri} (K)	m
0.00	7.31	10
0.25	7.24	11
0.50	7.31	11
0.75	8.26	10
1.00	9.48	10
1.25	11.42	10
1.50	13.02	10
2.00	14.75	15

force and induce an azimuthal flow of the melt layer, which can suppress the radial flow and retard flow instability. Therefore, ΔT_{cri} increases with the increasing the rotation rate.

During the determination of the critical temperature difference and wave number, non-uniform staggered grids of $62^r \times 20^z \times 163^\theta$ and $82^r \times 24^z \times 243^\theta$ are used with finer meshes in the regions under the free surface and near the bottom and sidewalls for $n = (0–1.5)$ rpm and $n = 2$ rpm, respectively. The azimuthal direction has uniform grids in all cases. In order to check the grid convergence, simulations with the different meshes are performed for $n = 1$ rpm and 2 rpm. Results are shown in Table 2, which confirm a good grid convergence.

3.3. The first hydrothermal waves

In following sections, non-uniform staggered grid of $62^r \times 20^z \times 163^\theta$ is used in all cases. In order to save calculation time, we always used the result of a small ΔT as initial condition when increasing ΔT, and the result of a large ΔT as one when decreasing ΔT.

Fig. 3 shows simulation results, including the snapshots of distribution of surface temperature fluctuation δT and a space-time diagram (STD) of surface temperature along a circumference at $r = 20$ mm. The surface temperature fluctuation δT is introduced in order to extract the 3D disturbances:

$$\delta T(r,\theta,d,t) = T(r,\theta,d,t) - \frac{1}{2\pi}\int_0^{2\pi} T(r,\theta,d,t)\,\mathrm{d}\theta. \qquad (10)$$

Table 2
Effect of meshes on critical condition

Meshes	ΔT (K)	m
n = 1 rpm		
$62^r \times 20^z \times 163^\theta$	9.48	10
$82^r \times 26^z \times 123^\theta$	9.78	10
$62^r \times 20^z \times 123^\theta$	9.85	10
$62^r \times 20^z \times 95^\theta$	11.98	9
$62^r \times 20^z \times 63^\theta$	15.37	3
n = 2 rpm		
$82^r \times 24^z \times 243^\theta$	14.75	15
$82^r \times 24^z \times 203^\theta$	15.05	15
$62^r \times 20^z \times 123^\theta$	17.98	8

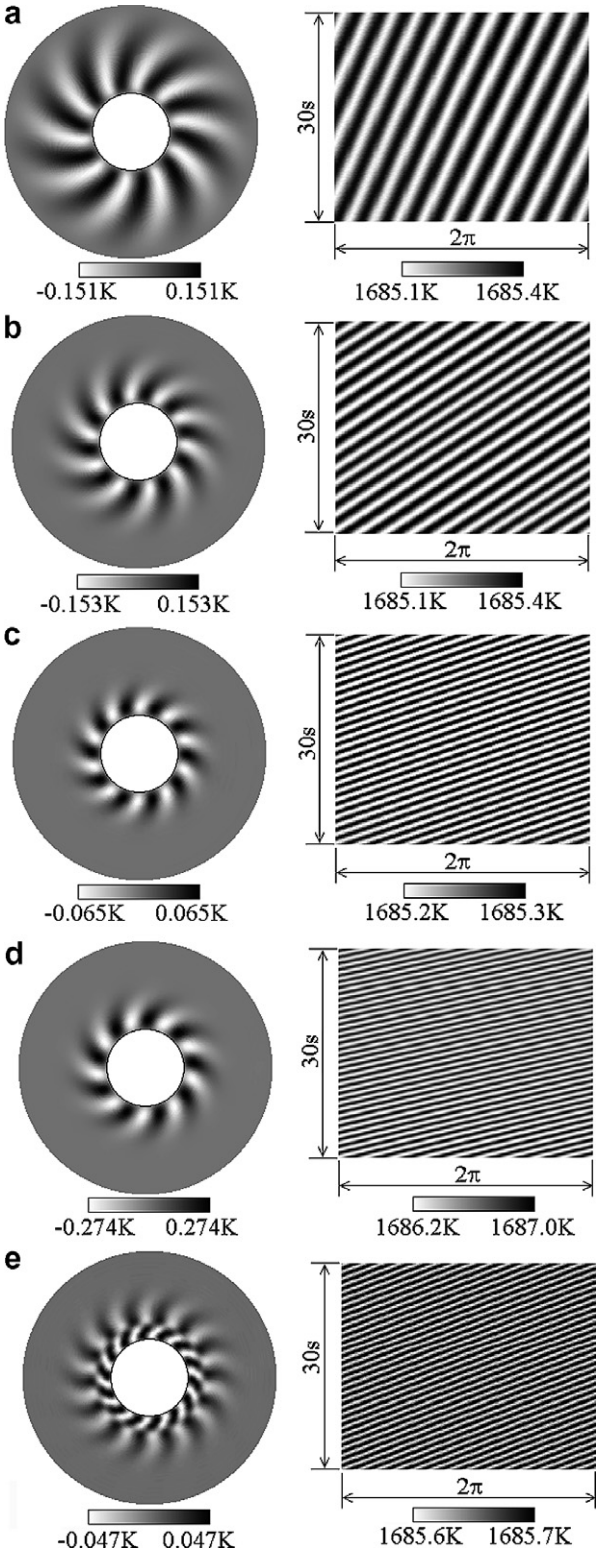

Fig. 3. Snapshots of surface temperature fluctuation (left side) and space-time diagram of surface temperature distribution (right side). (a) $n = 0$ rpm, $\Delta T = 10$ K. (b) $n = 0.5$ rpm, $\Delta T = 10$ K. (c) $n = 1.0$ rpm, $\Delta T = 10$ K. (d) $n = 1.5$ rpm, $\Delta T = 16$ K. (e) $n = 2.0$ rpm, $\Delta T = 16$ K.

Slightly above the critical condition, the hydrothermal wave instability is dominant and many traveling curved

spoke patterns are observed on the entire surface. In this case, these hydrothermal waves propagate in the counterclockwise direction. The angle (ϕ) between wave propagation and the radial direction, measured at $r = 20$ mm, is about 75–80° for $n = (0–1.5)$ rpm, Which is close to the angle of 80° predicted by the linear stability theory for infinite rectangular layer [1]. When $n = 2$ rpm, there are two regions with the different angle ϕ, which are about 75–80° and around 25° near the outer sidewall and the inner sidewall, respectively. We refer to these hydrothermal waves as the first hydrothermal wave (HW1).

With the increasing the rotation rate, the hydrothermal waves propagation velocity increases. Therefore, the inclination angle of the STD of surface temperature along a circumference at $r = 20$ mm, which is composed of slope straight lines, becomes small.

3.4. Flow transition process

With further increasing ΔT, the amplitude of surface temperature fluctuation gradually increases. When ΔT exceeds another threshold value, the second flow pattern transition happened. Through this critical point, the wave number m decreases abruptly from 9 or 10 to 3, as shown in Figs. 4 and 5, and the frequency f of surface temperature fluctuation also decreases. We refer to these hydrothermal waves as the second hydrothermal wave (HW2). The second threshold ΔT values are 15 K, 19 K and 21 K for $n = 0.5$ rpm, 1.0 rpm and 1.5 rpm, respectively, when increasing ΔT. Fig. 6a shows temperature variation at monitoring point P ($r = 20$ mm, $z = 3$ mm and $\theta = 0$) as flow pattern transition from the HW1 to the HW2. Obviously, the period of flow pattern transition is very long.

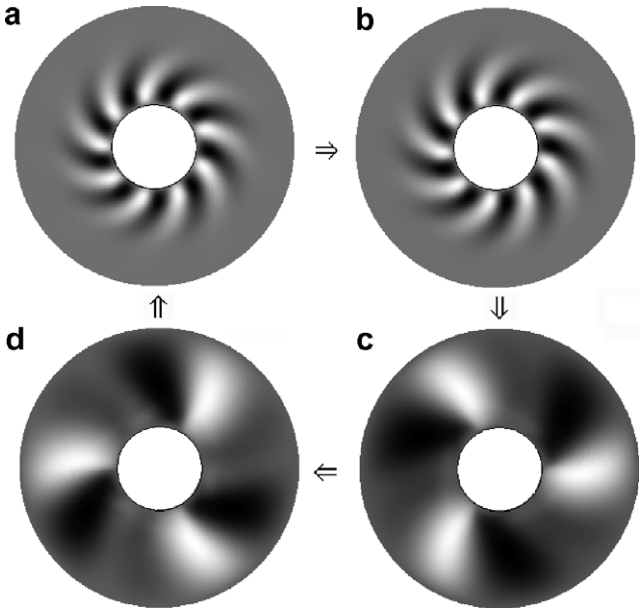

Fig. 4. Flow pattern transition between the HW1 and the HW2 at $n = 1$ rpm: (a) $\Delta T = 16$ K, (b) $\Delta T = 18$ K, (c) $\Delta T = 19$ K, and (d) $\Delta T = 17$ K.

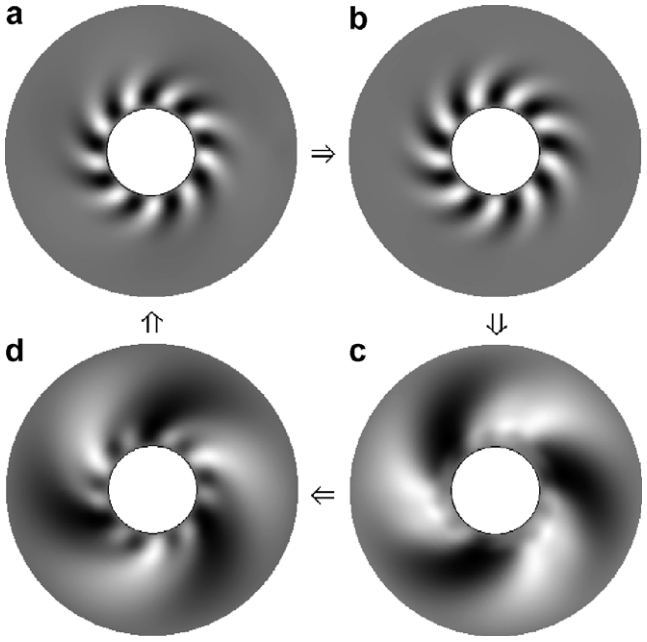

Fig. 5. Flow pattern transition between the HW1 and the HW2 at $n = 1.5$ rpm: (a) $\Delta T = 17$ K, (b) $\Delta T = 20$ K, (c) $\Delta T = 21$ K, and (d) $\Delta T = 18$ K.

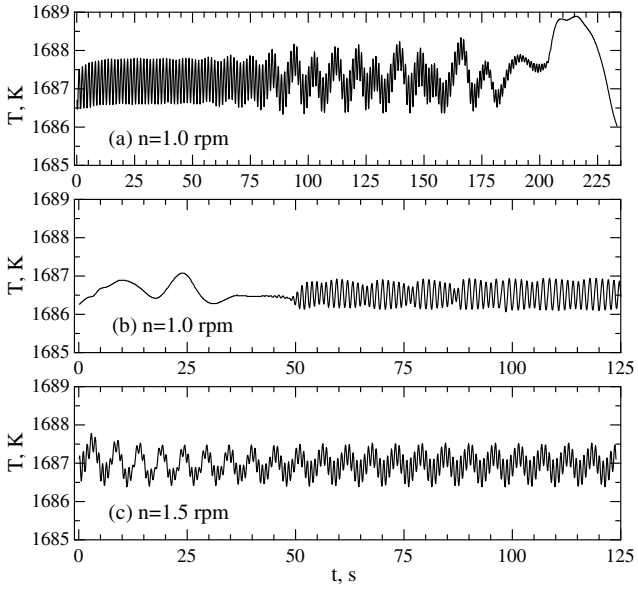

Fig. 6. Temperature variation at monitoring point P as flow transition between the HW1 and the HW2. (a) Increasing ΔT from 18 K to 19 K, (b) decreasing ΔT from 17 K to 16 K, and (c) decreasing ΔT from 19 K to 18 K.

Also, if we decrease the temperature difference, the HW2 becomes the HW1 again. But, the transition critical point is retarded. The transition ΔTs are 13 K, 16 K and 17 K for $n = 0.5$ rpm, 1.0 rpm and 1.5 rpm, respectively, when decreasing ΔT. The period of flow pattern transition becomes short, as shown in Fig. 6b and c. Therefore, the second transition between the HW1 and the HW2 exists

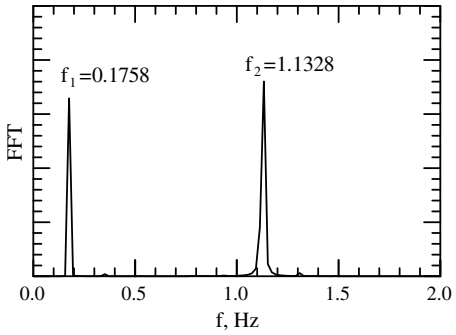

Fig. 7. Fourier spectra of temperature fluctuation at the monitoring point P at $n = 1.5$ rpm and $\Delta T = 18$ K.

hysteresis. The hysteretic temperature difference depends on the annular pool rotation rates.

During the flow pattern transition from the HW1 to the HW2 for $n = 1.5$ rpm, There coexist the HW1 and the HW2 in the transition zone. Fig. 6c shows temperature variation at monitoring point P as decreasing ΔT from 19 K to 18 K. Fig. 7 gives the results of Fourier spectra of temperature fluctuations, in which f_1 corresponds to the HW2 and f_2 to the HW1.

3.5. The second hydrothermal waves

When the temperature difference exceeds the second critical value, the HW2 appears on the free surface. In this case the wave number m is 3, as shown in Fig. 8. But, the propagating direction of the traveling waves depends on the rotation rates of the annular pool. For the case of $n = 0.5$ rpm, the traveling waves propagate along the clockwise direction. When $n = 1.0$ rpm, the azimuthal flow velocity of the melt layer driven by the annular pool rotation is almost same as the traveling wave velocity in the opposite direction. In this case, the traveling waves seem stable in a fixed frame. Thus, the STD taken at $r = 20$ mm is almost composed of the vertical straight lines. Under a much higher rotation rate, for example, $n = 1.5$ rpm, the flow driven by the annular pool rotation is dominant and the traveling waves propagate along the counter-clockwise direction. The traveling velocity of waves increases with the increasing the rotation rate of the annular pool.

3.6. Stability diagram

Fig. 9 shows the variation of the traveling velocity n_w of the waves with the temperature difference ΔT for the case of $n = 1$ rpm. In the region of small ΔT, the hydrothermal waves appear and have the high traveling velocity. When the ΔT exceeds the second critical value, the HW2 appears and has very low traveling velocity.

As described in the previous parts, the basic flow is the axisymmetric steady flow if the temperature difference ΔT is small. Over this basic flow, instability appears depending on the ΔT and n. To clarify the flow transitions we present the stability diagram, as shown in Fig. 10. Depending on the values of ΔT and n, four zones of the flow patterns can be distinguished: 2D stationary flow, the HW1, transition zone and the HW2.

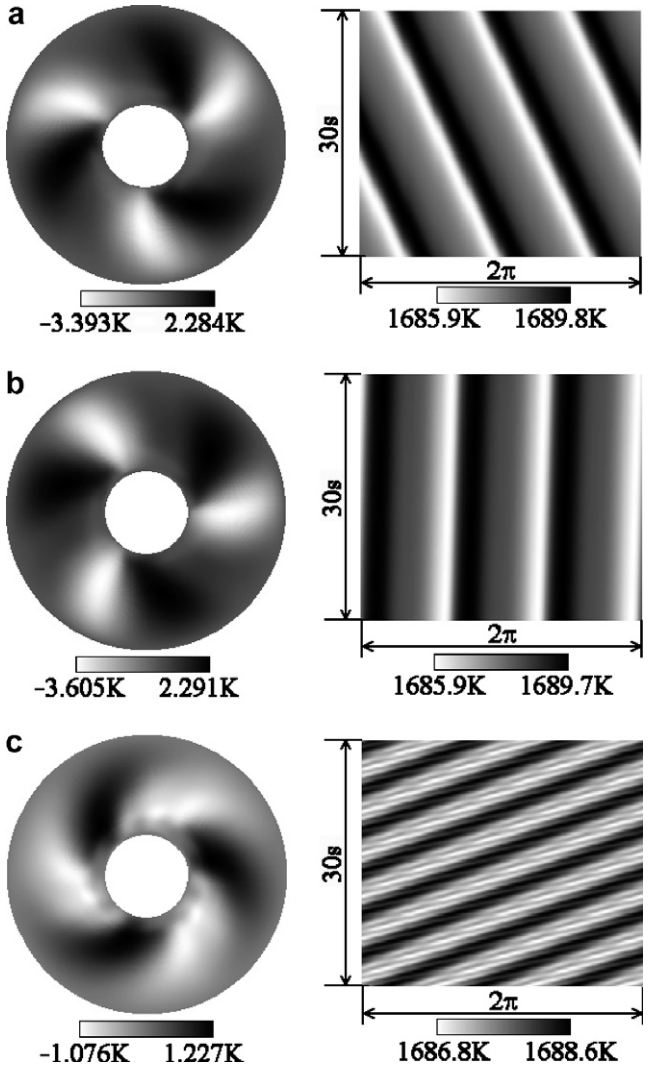

Fig. 8. Snapshots of surface temperature fluctuation (left side) and space-time diagram of surface temperature distribution (right side) at $\Delta T = 21$ K: (a) $n = 0.5$ rpm, (b) $n = 1.0$ rpm, and (c) $n = 1.5$ rpm.

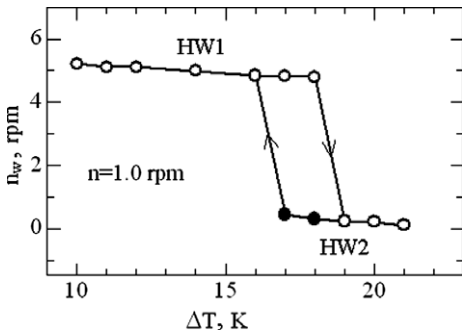

Fig. 9. Variation of traveling velocity of waves.

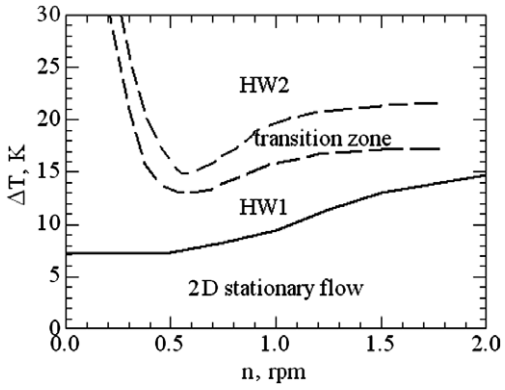

Fig. 10. Stable diagram of temperature difference ΔT versus rotation rate n.

4. Conclusions

A series of 3D numerical simulations of the thermocapillary flows in shallow annular pools of silicon melt with slow rotation rate were conducted by means of the control volume method. Simulations were conducted for a small annular melt pool ($r_o = 50$ mm and $r_i = 15$ mm and $d = 3$ mm). From the simulation results, the following conclusions were obtained.

1. The critical temperature differences for transition from an axisymmetric steady flow to the hydrothermal waves in each case were determined. The critical temperature difference depends on the annular pool rotation rate.
2. The hydrothermal waves propagate along the counterclockwise direction. The traveling velocity increases with the increasing the annular pool rotation rate.
3. The propagating direction of the traveling waves depends on the rotation rate of the annular pool in the oscillatory 3D flow. When the rotation rate is slow, the waves propagated in a direction opposite to the annular pool rotation. At higher rotation rate they have the same direction.
4. The stability diagram is presented and four flow zones are distinguished.

Acknowledgements

This work is supported by National Natural Science Foundation of China (Grant number 50476042) and the Scientific Research Foundation for the Returned Overseas Chinese Scholars, State Education Ministry [2003] 406-2. Ms. Li Zhang gave a lot of help for preparing the manuscript.

References

[1] M.K. Smith, S.H. Davis, Instabilities of dynamic thermocapillary liquid layers. Part 1. Convective instabilities, J. Fluid Mech. 132 (1983) 119–144.
[2] N. Garnier, C. Normand, Effect of curvature on hydrothermal waves instability of radial thermocapillary flows, C. R. Acad. Paris Part 2 Series IV-Phys. 2 (2001) 1227–1233.
[3] A. Zebib, Thermocapillary instabilities with system rotation, Phys. Fluids 8 (1996) 3209–3211.
[4] C. Le Cunff, A. Zebib, Thermocapillary-coriolis instabilities in liquid bridges, Phys. Fluids 11 (1999) 2539–2547.
[5] Y. Kamotani, S. Ostrach, A. Pline, Analysis of velocity data taken in surface tension driven convection experiment in microgravity, Phys. Fluids 6 (1994) 3601–3609.
[6] Y. Kamotani, S. Ostrach, J. Masud, Oscillatory thermocapillary flows in open cylindrical containers induced by CO_2 laser heating, Int. J. Heat Mass Transfer 42 (1999) 555–564.
[7] Y. Kamotani, Thermocapillary flow under microgravity – experimental results, Adv. Space Res. 24 (1999) 1357–1366.
[8] N. Mukolobwiez, A. Chiffaudel, F. Daviaud, Supercritical Eckhaus instability for surface-tension-driven hydrothermal waves, Phys. Rev. Lett. 80 (1998) 4661–4664.
[9] D. Schwabe, U. Moller, J. Schneider, A. Scharmann, Instabilities of shallow dynamic thermocapillary liquid layers, Phys. Fluids A 4 (1992) 2368–2381.
[10] N. Garnier, A. Chiffaudel, Two dimensional hydrothermal waves in an extended cylindrical vessel, Eur. Phys. J. B 19 (2001) 87–95.
[11] D. Schwabe, S. Benz, Thermocapillary flow instabilities in an annulus under microgravity – results of the experiment MAGIA, Adv. Space Res. 29 (2002) 629–638.
[12] D. Schwabe, A. Zebib, B.C. Sim, Oscillatory thermocapillary convection in open cylindrical annuli. Part 1. Experiments under microgravity, J. Fluid Mech. 491 (2003) 239–258.
[13] J.S. Fein, R.L. Pfeffer, An experimental study of the effects of Prandtl number on thermal convection in a rotating, differentially heated cylindrical annulus of fluid, J. Fluid Mech. 75 (1976) 81–112.
[14] A. Seidl, G. McCord, G. Muller, H.L. Leister, Experimental observation and numerical simulation of wave patterns in a Czochralski silicon melt, J. Crystal Growth 137 (1974) 326–334.
[15] S. Nakamura, M. Eguchi, T. Azami, T. Hibiya, Thermal waves of a nonaxisymmetric flow in a Czochralski-type silicon melt, J. Crystal Growth 207 (1999) 55–61.
[16] T. Azami, S. Nakamura, M. Eguchi, T. Hibiya, The role of surface-tension-driven flow in the formation of a surface pattern on a Czochralski silicon melt, J. Crystal Growth 233 (2001) 99–107.
[17] B.C. Sim, A. Zebib, Effect of free surface heat loss and rotation on transition to oscillatory thermocapillary convection, Phys. Fluids 14 (2002) 225–231.
[18] B.C. Sim, A. Zebib, D. Schwabe, Oscillatory thermocapillary convection in open cylindrical annuli. Part 2. Simulations, J. Fluid Mech. 491 (2003) 259–274.
[19] Y.R. Li, L. Peng, Y. Akiyama, N. Imaishi, Three-dimensional numerical simulation of thermocapillary flow of moderate Prandtl number fluid in an annular pool, J. Crystal Growth 259 (2003) 374–387.
[20] W.Y. Shi, N. Imaishi, Hydrothermal waves in differentially heated shallow annular pools of silicone oil, J. Crystal Growth 290 (2006) 280–291.
[21] Y.R. Li, N. Imaishi, T. Azami, T. Hibiya, Three-dimensional oscillatory flow in a thin annular pool of silicon melt, J. Crystal Growth 260 (2004) 28–42.
[22] Y.R. Li, N. Imaishi, L. Peng, S.Y. Wu, T. Hibiya, Thermocapillary flow in a shallow molten silicon pool with Cz configuration, J. Crystal Growth 266 (2004) 88–95.
[23] Y.R. Li, X.J. Quan, L. Peng, N. Imaishi, S.Y. Wu, D.L. Zeng, Three-dimensional thermocapillary-buoyancy flow in a shallow molten silicon pool with Cz configuration, Int. J. Heat Mass Transfer 48 (2005) 1952–1960.